IEEE Access
Multidisciplinary | Rapid Review | Open Access Journal

Received April 28, 2020, accepted May 10, 2020, date of publication May 25, 2020, date of current version March 8, 2021.

Digital Object Identifier 10.1109/ACCESS.2020.2997256

Wide-Angle Frequency-Scanning Array Antenna Using Dual-Layer Finger Connected Interdigital Capacitor Based CRLH Unit Cell

BIN-FENG ZONG, HUI-YONG ZENG, FAN WU, GUANG-MING WANG, (Member, IEEE), AND LIN GENG

Air Force Engineering University, Xi'an 710051, China

Corresponding author: Hui-Yong Zeng (hyzeng.1023@163.com)

This work was supported in part by the National Natural Science Foundation of China under Grant 61701527, and in part by the National Natural Science Foundation of Shaanxi Province under Grant 2020JQ-482.

ABSTRACT In this paper, a wide-angle frequency-scanning array antenna is presented for three-dimensional (3D) radar. Initially, a modified composite right/left-handed (CRLH) unit cell based on a dual-layer finger-connected interdigital capacitor (FCIDC) is analyzed. Compared with its conventional counterpart, the proposed unit cell eliminates the undesired high-order resonances and has a lower right/left-handed passband. Then, a broadband frequency-scanning feeding network, which has a large scanning angle, is designed using the proposed CRLH unit cell. The responses of the four output ports indicate that the network can offer desired amplitude and phase difference to scan towards both negative and positive elevation angles. To validate its performance, a tightly coupled planar quasi-Yagi antenna array is fed to synthesize an array antenna. The measured results show that the designed array antenna has an impedance bandwidth ($|S_{11}| < -10$ dB) of 118.7% (2.55-10 GHz) and gains larger than 5dBi in the bulk of the band. Besides, the radiated beam can scan from $-47°$ to $46°$ continuously when the frequency ranges from 3GHz to 9GHz.

INDEX TERMS FCIDC, CRLH, wide-angle, frequency-scanning networks, dual-layer.

I. INTRODUCTION

Frequency-scanning antenna array presents its good potential in three-dimensional (3D) radar, because of its many advantages such as low cost, stable operation and large scanning beam angles. In recent years, it has been studied extensively because the radiated directions of the antenna array vary with the frequencies. Leaky-wave antenna (LWA) is a general type of frequency beam scanning antennas [1]. It consists of a travelling wave structure that radiates power along its length gradually. It can be described by two parameters including a phase constant and a leakage factor.

Until now, many techniques have been used for LWAs design. Microstrip technique is an initial method in leaky-wave antenna design. In [2], a microstrip-based backfire planar LWA, which exhibits high radiation efficiency and low cross-pol level, is presented. Recently, spoof surface plasmon polaritons transmission lines (SSPPs-TLs) have been a good choice to design LWAs. In [3] and [4], SSPPs-TLs have been used as guiding-wave structures for broad scanning-angle LWAs. Besides, substrate integrated waveguide (SIW) technology can also be applied in the design of LWAs. In [5], a new class of SIW-based LWAs, which can scan the beam continuously from backward to forward direction, is proposed to overcome the open stopband problem of unidirectional periodic LWAs to scan the beam through the broadside direction. And a dual-band SIW slotted LWA is presented in [6]. It is composed of two back-to-back quasi-uniform slotted SIW arrays fed by a stirp line. In [7], a dual-band and dual-polarized leaky-wave antenna excited by slotted SIW has been proposed. It achieves beam scanning from $+107°$ to $+167°$ at the lower band and from $-41°$ to $-114°$ at the higher one. In [8], a broadband frequency scanning antenna with considerable gain is synthesized using TE220 mode in SIW technology. Eighth-mode SIW also presents good performance in LWA design and a high gain wide full space scanning LWA with improved broadside radiation profile has been presented in [9]. Additionally, metasurfaces have been

The associate editor coordinating the review of this manuscript and approving it for publication was Yasar Amin.

used to design LWAs [10]–[13]. In [10] and [11], a novel concept of a leaky-wave antenna is proposed using the Huygens' metasurfaces. With the appearance of CRLH-metamaterial, the LWAs can realize a new function of generating alterable patterns in different frequencies [14]–[17]. Creatively, an LWA, which can provide beam scanning from backfire to endfire, has been designed using CRLH-metamaterial in [14] firstly. Balanced CRLH-TLs are good choice to design broadside radiation without stop band between the left-handed (LH) region and the right one. And then, a LWA with minimized sidelobe levels is designed in [15]. In [16], a wide-area innovative beam-scanning LWA for millimetre-wave applications is designed based on CRLH-metamaterial. Although these antennas present good performances in leaky wave, the radiated type is determined when the structure is fixed. And these LWAs have an inherent disadvantage of low radiation efficiency.

Using the CRLH-TLs to design a feeding network provides a new method for frequency-scanning phased-array. In this way, the frequency-scanning functionality can be achieved rather than the antenna design. As a result, the antenna element can be chosen randomly and radiation property can be designed independently. The existence of CRLH-TLs feeding network results in less influence on radiation performance. However, few frequency-scanning phased-arrays using this method have been reported. As reported in [18], a feeding network, which operates in dual-band, has been designed using CRLH-TLs pioneering. And in [19], two frequency-scanning phased-arrays separately with equal and unequal amplitude output ports have been synthesized utilizing CRLH dispersive TLs. But all of them are fabricated complexly because the lumped elements have been used. In [20], a frequency-scanning feeding network, which has a large scanning angle ranging towards both negative and positive elevation angles in wide band, has been synthesized. However, the etched slot in ground results in difficulty of encapsulation. In [21], a planar 2-D antenna array, which can be used for radar or imaging applications with the appropriate transmit/receive circuitry, is designed using CRLH-TLs for series feeding network. But it can only operate in narrow band.

In this paper, a novel dual-layer performance-enhanced CRLH unit cell based on finger-connected (FC) technology is proposed previously. The proposed CRLH unit cell has a wide band due to the elimination of the spurious spikes and realizes a degree of miniaturization. And then, a frequency-scanning phased-array feeding network with low insertion loss and less phase difference is synthesized by combining conventional microstrip lines, modified CRLH lines and power dividers. To validate the properties of the new proposed feeding network, a tightly coupled quasi-Yagi antenna array is fed by the network. Both numerical and experimental results exhibit that the antenna array has a wide bandwidth of 2.55-10GHz and gains larger than 5dBi in the bulk of the band. Additionally, the scanning angle of the antenna is from $-47°$ to $46°$ between 3 GHz and 9 GHz. The designed array can be used in wideband radar systems that require a large scanning angle range.

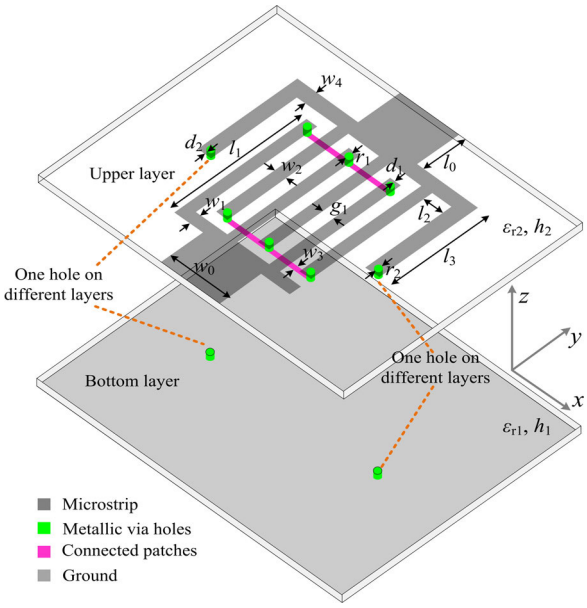

FIGURE 1. Layout of the proposed dual-layer FCIDC-based CRLH unit cell.

II. MODIFIED CRLH UNIT CELL

According to [22], the spurious spikes can be eliminated when the fingers of the IDC on the open end at the same port are connected. And a CRLH unit cell with wide operating frequency range has been designed using wire bonded IDC because the spurious spikes are eliminated. However, the wire bonded technology is difficult to fabricate. To tackle this problem, a new method is proposed in this paper. Fig. 1 shows the layout of the proposed dual-layer CRLH unit cell based on FCIDC. Unlike the CRLH unit cell in [23], the proposed one has metallic via holes at the open ends of all capacitor fingers. Two rectangular microstrip structures on the middle layer provide two patches to connect those via holes of the alternate fingers at the same port. The specific dimensions of the proposed CRLH unit cell are given as follows: $w_0 = 2.8$mm, $w_1 = 0.5$, $w_2 = 0.4$mm, $w_3 = 0.2$mm, $w_4 = 0.4$mm, $l_0 = 0.5$mm, $r_1 = 0.3$mm, $l_1 = 6.8$mm, $d_1 = 0.1$mm, $g_1 = 0.2$mm, $l_2 = 2.5$mm, $l_3 = 6.7$mm, $r_2 = 0.4$mm, $d_2 = 0.15$mm, $h_1 = 0.7$mm, $h_2 = 0.3$mm. Here, substrates with a dielectric constant of 2.65 and a loss tangent of 0.001 have been used.

Fig. 2 (a) presents the lumped equivalent circuit model of the IDC-based CRLH unit cell. A finger can be represented by a series inductance L_i ($i = 1, 2\ldots, 6$) and a shunt capacitance. In this model, the shunt capacitances are not shown for the sake of clarity. The capacitive coupling is modeled by the capacitances C_{mn}, where m and n are the finger numbers. As reported in [24], the inductive coupling can be ignored in a first approximation. The shunt stubs are represented by the shunt resonant circuits composed of L_0 and C_0. Fig. 2 (b) shows the circuit model of the FCIDC- based CRLH unit cells. The application of microstrip patches can make a new

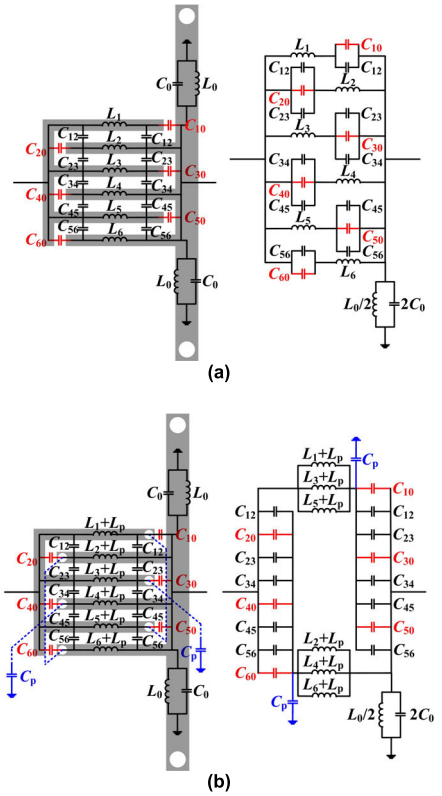

FIGURE 2. Equivalent circuit models of the CRLH unit cells. (a) IDC-based CRLH unit cell. (b) FCIDC-based CRLH unit cell.

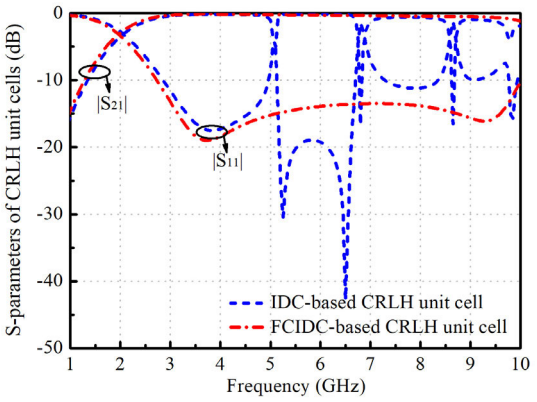

FIGURE 3. Simulated S-parameters of IDC- and FCIDC-based CRLH unit cells.

arrangement of lumped elements in conventional IDC. In this circuit model, the rectangular slot rings on the ground provide the capacitances C_p and the via holes at the open ends of the capacitor fingers provide the inductances L_p. It can be seen that the circuit model in Fig. 2 (b) has fewer series resonant branches than that in Fig. 2 (a), which reveals that the new CRLH-TL has fewer spurious spikes. According to these two comparable circuit models, the improved mechanism is illustrated clearly when the patches are used to connect the fingers at the same port. Here, it should be pointed out that the common dimensions of the CRLH unit cells based on the FCIDC and the conventional IDC are the same.

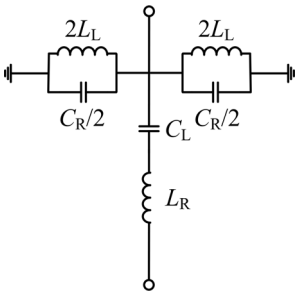

FIGURE 4. Lumped equivalent circuit model of the CRLH unit cell.

Fig. 3 presents the simulated S-parameters of IDC- and FCIDC-based CRLH unit cells. From Fig. 3, it can be observed that the IDC-based CRLH unit cell has four spurious spikes at 5.1 GHz, 6.8 GHz, 8.65GHz and 9.8 GHz respectively, which prevents the IDC from being used beyond 5.1 GHz. Conversely, the spurious spikes are eliminated when the fingers of IDC at the same port are connected. As a result, the FCIDC-based CRLH unit cell obtains a wide operating band. Besides, the lower frequency of the pass band is smaller than that of its conventional counterpart, which indicates that the proposed CRLH unit cell has an advantage of miniaturization.

In order to explain the mechanism of the miniaturization clearly, a classical lumped equivalent circuit model in Fig. 4 is used. The model in Fig. 2 is too complex to explain the phenomenon and a simple one is more effective, but the spurious spikes are not considered in this model. The model consists of a series *LC* tanks and two parallel *LC* tanks. The parallel *LC* tanks, which are composed of L_L and C_R, represent the shunt grounded stub in Fig.1. And the series *LC* tank, which is composed of L_R and C_L, represents the FCIDC. C_L and L_R are the total series capacitance and total series inductance of the unit cells, and L_L and C_R are separated from the total shunt capacitance and inductance.

Based on the classical circuit theory in [24], the values of the lumped elements can be calculated roughly. Then, through putting them as initial values and using the above *S*-parameters as optimization objectives, the final values of the lumped elements can be extracted using the Optimization Dialog Box in *Serenade*.

The extracted values of these elements for IDC-based CRLH unit cell are: $C_L = 0.79$pF, $L_R = 2.72$nH, $C_R = 1.08$pF, $L_L = 1.85$nH. And the extracted values of these elements for the CRLH unit cell based on the FCIDC are: $C_L = 0.92$pF, $L_R = 2.88$nH, $C_R = 1.27$pF, $L_L = 1.86$nH. From the extracted results of IDC- and FCIDC-based CRLH unit cells, we can know that larger series inductance L_R, series capacitance C_L and shunt capacitance C_R can be obtained when the FCIDC is used. The via holes at the open ends of the capacitor fingers provide extra inductances L_p for L_R, and the patches on the ground provide additional capacitances C_p for C_R.

The new arrangement of C_{mn} results in a larger C_L because all C_{mn} of the IDC make contribution to them. Besides, the

patches enhance the mutual coupling of the fingers, which can increase the values of C_{mn}. As a result, a larger C_{L} can be obtained. The left/right-handed pass band can be calculated as [25]:

$$\omega_{cL} < \omega < \max(\omega_{se}, \omega_{sh}) \quad \text{(LH pass band)} \tag{1}$$

$$\max(\omega_{se}, \omega_{sh}) < \omega < \omega_{cR} \quad \text{(RH pass band)} \tag{2}$$

where,

$$\omega_{cL} = \omega_0 \sqrt{\left\{[\kappa + (2/\omega_L)^2]\omega_0^2 - \sqrt{[\kappa + (2/\omega_L)^2]^2\omega_0^4 - 4}\right\}/2}$$

$$\omega_{cR} = \omega_0 \sqrt{\left\{[\kappa + (2/\omega_L)^2]\omega_0^2 + \sqrt{[\kappa + (2/\omega_L)^2]^2\omega_0^4 - 4}\right\}/2}$$

$$\kappa = L_R C_L + L_L C_R \quad \omega_0 = \sqrt{\omega_{se}\omega_{sh}}$$

$$\omega_{se} = 1/\sqrt{L_R C_L} \quad \omega_{se} = 1/\sqrt{L_L C_R}$$

According to Eqs.(1) and (2), the operating LH and RH pass bands are shifted downward because the application of FCIDC provides larger L_{R}, C_{L} and C_{R}. This indicates that the CRLH unit cell based on the FCIDC can realize a degree of miniaturization.

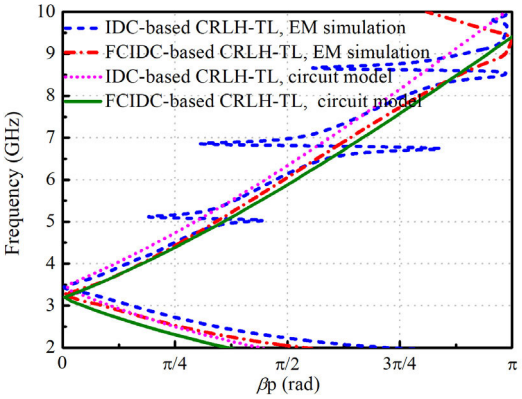

FIGURE 5. Comparison among dispersion curves of EM and circuit models for the two CRLH unit cells.

Fig. 5 presents the dispersion curves of IDC- and FCIDC-based CRLH unit cells by full-wave simulation and equivalent circuit model. It can be observed that the FCIDC-based CRLH unit cell has a lower LH pass band. The spurious spikes of the conventional IDC-based CRLH unit cell are not achieved in its circuit model, because the circuit model just provides an approximate solution and some of parasitic elements are ignored for the sake of simplicity. The CRLH can provide phase advance and phase delay in LH band and RH band, simultaneously.

The FCIDC-based CRLH unit cell has a wider operating bandwidth, because the spurious spikes of its conventional counterpart are eliminated using the proposed method. Additionally, it has a smaller electric size compared with the conventional one, because the new cell has a lower LH pass band. As a result, the novel CRLH unit cell can be applied to design devices with a wider phase response and small size.

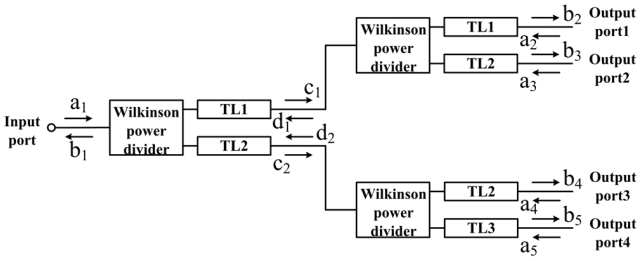

FIGURE 6. Sketch map of a frequency-scanning feeding network.

III. WIDEBAND FREQUENCY-SCANNING FEEDING NETWORK

A. TOPOLOGY OF FREQUENCY-SCANNING NETWORK

Fig. 6 exhibits the sketch map of the frequency-scanning feeding network. It can be seen that the network is composed of three power dividers and six phase shift lines. a_i, d_m (i = 1,2,3,4,5; m = 1,2) are normalized incident wave voltages and b_i, c_m (i = 1,2,3,4,5; m = 1,2) are normalized reflection wave voltages. According to the microwave network principle [26], the S-parameters of a power divider can be expressed as

$$S_{\mathrm{wilk.}} = \frac{-j}{\sqrt{2}} \begin{bmatrix} 0 & 1 & 1 \\ 1 & 0 & 0 \\ 1 & 0 & 0 \end{bmatrix} \tag{3}$$

Assuming that the phase shift of line 1, line 2 and line 3 are $\varphi_1(f)$, $\varphi_2(f)$ and $\varphi_3(f)$ at the frequency of f, respectively. So, their S-matrix $[S]_A$, $[S]_B$, $[S]_C$ can be calculated as

$$[S]_A = \begin{bmatrix} 0 & e^{j\varphi_1(f)} \\ e^{j\varphi_1(f)} & 0 \end{bmatrix} \tag{4}$$

$$[S]_B = \begin{bmatrix} 0 & e^{j\varphi_2(f)} \\ e^{j\varphi_2(f)} & 0 \end{bmatrix} \tag{5}$$

$$[S]_C = \begin{bmatrix} 0 & e^{j\varphi_3(f)} \\ e^{j\varphi_3(f)} & 0 \end{bmatrix} \tag{6}$$

Based on expressions (3), (4), (5) and (6), the following relations for the frequency-scanning feeding network can be obtained

$$\begin{cases} \mathrm{b}_1 = \dfrac{-j}{\sqrt{2}}\left(\mathrm{d}_1 e^{j\varphi_1(f)} + \mathrm{d}_2 e^{j\varphi_2(f)}\right) \\ \mathrm{c}_1 = \dfrac{-j}{\sqrt{2}}\mathrm{a}_1 e^{j\varphi_1(f)} \\ \mathrm{c}_2 = \dfrac{-j}{\sqrt{2}}\mathrm{a}_1 e^{j\varphi_2(f)} \end{cases} \tag{7}$$

$$\begin{cases} \mathrm{d}_1 = \dfrac{-j}{\sqrt{2}}\left(\mathrm{a}_2 e^{j\varphi_1(f)} + \mathrm{a}_3 e^{j\varphi_2(f)}\right) \\ \mathrm{b}_2 = \dfrac{-j}{\sqrt{2}}\mathrm{c}_1 e^{j\varphi_1(f)} \\ \mathrm{b}_3 = \dfrac{-j}{\sqrt{2}}\mathrm{c}_1 e^{j\varphi_2(f)} \end{cases} \tag{8}$$

$$\begin{cases} d_2 = \dfrac{-j}{\sqrt{2}}\left(a_4 e^{j\varphi_2(f)} + a_5 e^{j\varphi_3(f)}\right) \\ b_4 = \dfrac{-j}{\sqrt{2}} c_2 e^{j\varphi_2(f)} \\ b_5 = \dfrac{-j}{\sqrt{2}} c_2 e^{j\varphi_3(f)} \end{cases} \tag{9}$$

Combining the expressions (7), (8) and (9), the relation between the normalization incident wave voltages a_i and normalization reflection wave voltages b_i of the frequency-scanning feeding network can be achieved. Consequently, the *S*-parameters of the frequency-scanning feeding network can be expressed as (10), shown at the bottom of this page.

Based on (10), the amplitudes of the four output ports of the network are the same and the phase responses of output ports from 1, 2, 3 and 4 are $2\varphi_1(f)$, $\varphi_1(f)+\varphi_2(f)$, $2\varphi_2(f)$ and $\varphi_2(f)+\varphi_3(f)$. So, the phase differences of the adjacent output ports can be calculated as $\Delta\varphi_1(f) = \varphi_2(f) - \varphi_1(f)$, $\Delta\varphi_2(f) = \varphi_2(f) - \varphi_1(f)$, $\Delta\varphi_3(f) = \varphi_3(f) - \varphi_2(f)$. To design a proper network, two conditions should be satisfied. On one hand, the phase differences of the adjacent output ports should be equal at arbitrary frequency. Namely, $\Delta\varphi_1(f) = \Delta\varphi_2(f) = \Delta\varphi_3(f)$. On the other hand, the phase differences should be continuous. Fig. 7 illustrates the ideal phase relations between the phase shifts TLs. According to Fig. 7, it is required that $\Delta\varphi_2(f) = \Delta\varphi_3(f)$. It can be also seen that the phase differences toward from negative to positive as frequency shifts away from ω_0. Extra, the frequency-scanning feeding network designed in this method can reduce the number of TLs effectively.

B. CRLH TLs

Fig. 8 illustrates the beam direction with variable phase difference. In this figure, d is the distance of adjacent elements and θ is the beam angle. The phase difference is a function of the frequency f_i. *MM*' and *PP*' are the equal phase surfaces as the beam angle are θ and $-\theta$, respectively. Assuming that the beam angle is θ at f_1, and the beam angle is $-\theta$ at f_2. For an antenna array designing, the coupling between the antenna elements and the grating lobe should be considered comprehensively [27]. Generally, the grating lobe is more crucial. On the basis of [28], the maximum inter-element spacing is set as

$$d_{\max} < \frac{c}{f_2\,(1 + |\sin\theta|)} \tag{11}$$

c is velocity of light. The phase difference at random frequency can be calculated as

$$\Delta\varphi(f_i) = \varphi_j(f_i) - \varphi_{j-1}(f_i) = -\frac{2\pi f_i}{c} d_{\max}\sin\theta \quad i = 1, 2; \quad j = 2, 3\ldots, N \tag{12}$$

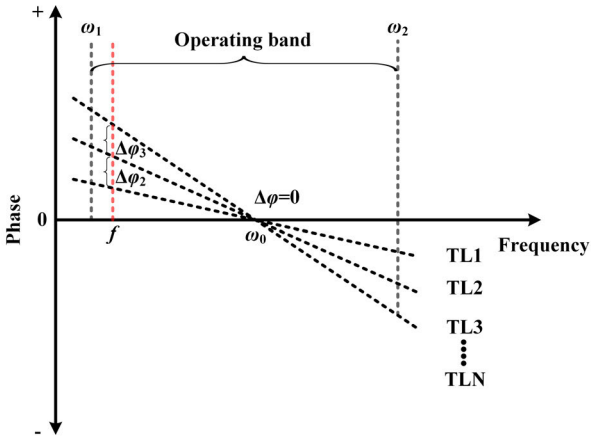

FIGURE 7. Ideal phase relationships between the TLs.

For phase shift lines design, three factors of antenna array including the bandwidth, the scale of beam angle and the element spacing should be taken into consideration. In this paper, the feeding network is designed to scan from $-45°$ to $45°$ as $f_1 = 3$GHz and $f_2 = 9$GHz. Using expression (11), it can be calculated that the value of $d_{\max}$ should be less than 19.53 mm to avoid grating lobe. So, the distance is chosen as 19.5 mm. Substituting this value into (12), $\Delta\varphi(f_1) = 49.64°$ and $\Delta\varphi(f_2) = -148.92°$. Here, the values of the lumped elements should satisfy the equations in (13).

$$\begin{cases} L_R = \dfrac{Z_0\left[\left(\frac{f_1}{f_2}\right)\psi_1 - \psi_2\right]}{n2\pi f_2\left[1 - \left(\frac{f_1}{f_2}\right)^2\right]} \\ C_R = \dfrac{\left(\frac{f_1}{f_2}\right)\psi_1 - \psi_2}{n2\pi f_2 Z_0\left[1 - \left(\frac{f_1}{f_2}\right)^2\right]} \\ L_L = \dfrac{nZ_0\left[1 - \left(\frac{f_1}{f_2}\right)^2\right]}{2\pi f_1\left[\psi_1 - \left(\frac{f_1}{f_2}\right)\psi_2\right]} \\ C_L = \dfrac{n\left[1 - \left(\frac{f_1}{f_2}\right)^2\right]}{2\pi f_1 Z_0\left[\psi_1 - \left(\frac{f_1}{f_2}\right)\psi_2\right]} \end{cases} \tag{13}$$

n is the number of CRLH unit cells. $\psi_1 = \Delta\varphi(f_1)$, $\psi_2 = \Delta\varphi(f_2)$ and $Z_0 = 50\Omega$. The values of L_R, C_R, L_L and C_L are 1.72nH, 0.69pF, 2.72nH and 1.09pF when n is equal to 2. In our design, two CRLH-TLs (TL2 and TL3 are shown in

$$[S] = \frac{-j}{2}\begin{bmatrix} 0 & e^{j2\varphi_1(f)} & e^{j(\varphi_1(f)+\varphi_2(f))} & e^{j2\varphi_2(f)} & e^{j(\varphi_2(f)+\varphi_3(f))} \\ e^{j2\varphi_1(f)} & 0 & 0 & 0 & 0 \\ e^{j(\varphi_1(f)+\varphi_2(f))} & 0 & 0 & 0 & 0 \\ e^{j2\varphi_2(f)} & 0 & 0 & 0 & 0 \\ e^{j(\varphi_2(f)+\varphi_3(f))} & 0 & 0 & 0 & 0 \end{bmatrix} \tag{10}$$

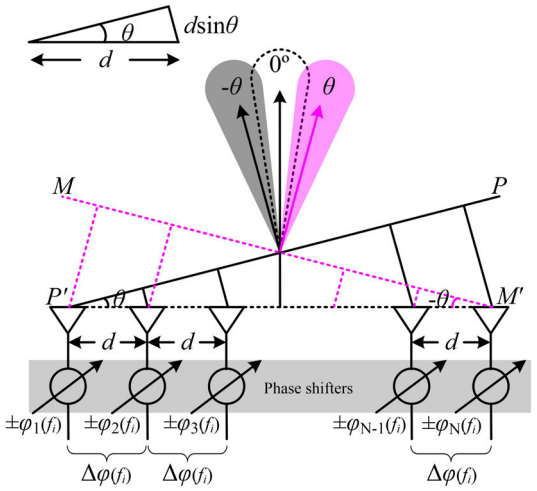

FIGURE 8. Beam direction with variable phase differences.

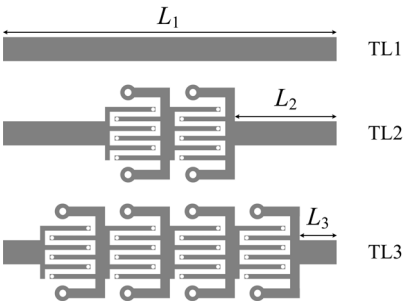

FIGURE 9. TLs based on FCIDC CRLH unit cells and their conventional counterpart.

Fig. 9, TL1 is the conventional one) are designed to realize required phase differences by a frequency feeding network. One is designed by cascading two unit cells and another is designed by cascading four unit cells. After optimizing, the dimensions of FCIDC-based CRLH unit cell in Fig. 8 are: $w_0 = 2.8$mm, $w_1 = 0.3$mm, $w_2 = 0.4$mm, $w_3 = 0.2$mm, $w_4 = 0.4$mm, $l_0 = 0.5$mm, $l_1 = 6.94$mm, $l_2 = 2.5$mm, $l_3 = 6.7$mm, $g_1 = 0.14$mm, $r_1 = 0.3$mm, $r_2 = 0.4$mm, $d_1 = 0.1$mm, $d_2 = 0.15$mm, $h_1 = 0.7$mm, $h_2 = 0.3$mm, $L_1 = 63.5$mm, $L_2 = 26.5$mm and $L_3 = 20.8$mm.

Fig. 10 presents the S-parameters of the TLs based on FCIDC-based CRLH unit cell and its conventional counterpart. The reflection coefficients of these three TLs are smaller than -10dB at the frequency ranging from 3GHz to 9GHz, and the insertion losses of them are less than 1dB in this band. Fig. 11 depicts the phase differences between the designed TLs. Here, $P_{(j)}(j = 1, 2, 3)$ is the phase responses of TL_j $(j = 1, 2, 3)$. At 4.7 GHz, the phase differences are 0°. The values of $P_{(3)} - P_{(2)}$ and $P_{(2)} - P_{(1)}$ are positive when the frequency is less than 4.7 GHz. Conversely, the values of $P_{(3)} - P_{(2)}$ and $P_{(2)} - P_{(1)}$ are negative when the frequency is larger than 4.7 GHz. Besides, the imbalance of phase differences is less than 4°. The phase differences ($P_{(3)} - P_{(2)}$ and $P_{(2)} - P_{(1)}$) are 49.3° and 51.2° at 3GHz. And the phase differences ($P_{(3)} - P_{(2)}$ and $P_{(2)} - P_{(1)}$) are −149.3° and −151.2° at 9GHz.

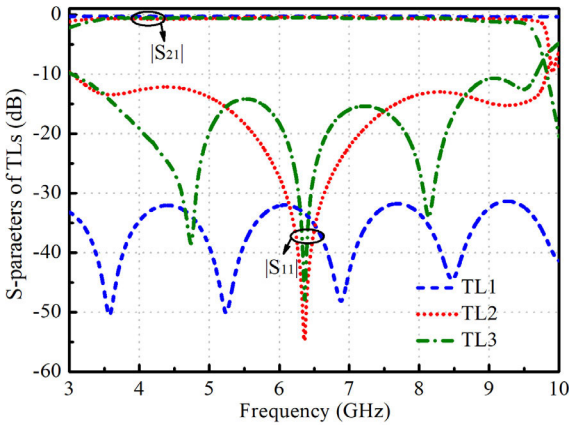

FIGURE 10. Simulated transmission coefficients and reflection coefficients of TLs.

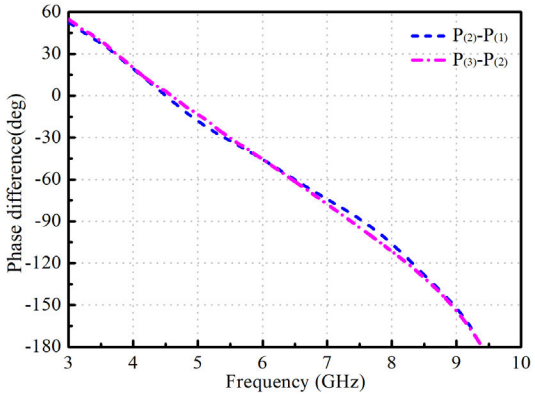

FIGURE 11. Phase differences of the designed TLs.

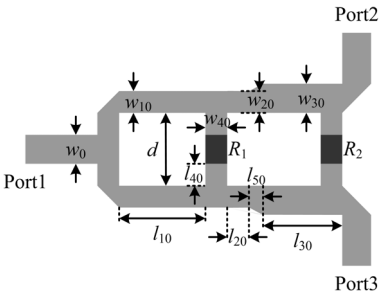

FIGURE 12. Structure of wideband Wilkinson power divider.

C. WIDEBAND WILKINSON POWER DIVIDER

A wideband power divider, whose topology is shown in Fig. 12, is designed for frequency-scanning network. Here, multi-section impedance converter is used to enhance the operating band, as the reflected wave arising from single section can be offset by other sections. The dimensions of the power divider are: $w_0 = 2.8$mm, $w_{10} = 1.3$mm, $l_{10} = 5.5$mm, $w_{20} = 1.3$mm, $l_{20} = 0.7$mm, $w_{30} = 2$mm, $l_{30} = 5.1$mm, $w_{40} = 1$mm, $l_{40} = 1.5$mm, $l_{50} = 1.5$mm, $d = 4.3$mm. R_1 and R_2 are isolation resistances. Their values are 100Ω and 200Ω, respectively.

Fig. 13 shows the simulated S-parameters of the designed power divider. It exhibits a −15 dB reflection coefficient

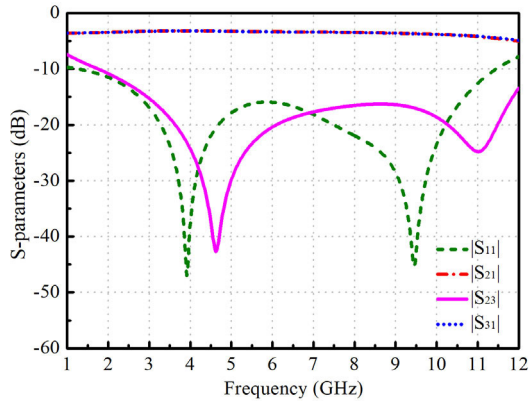

FIGURE 13. Simulated results of wideband Wilkinson power divider.

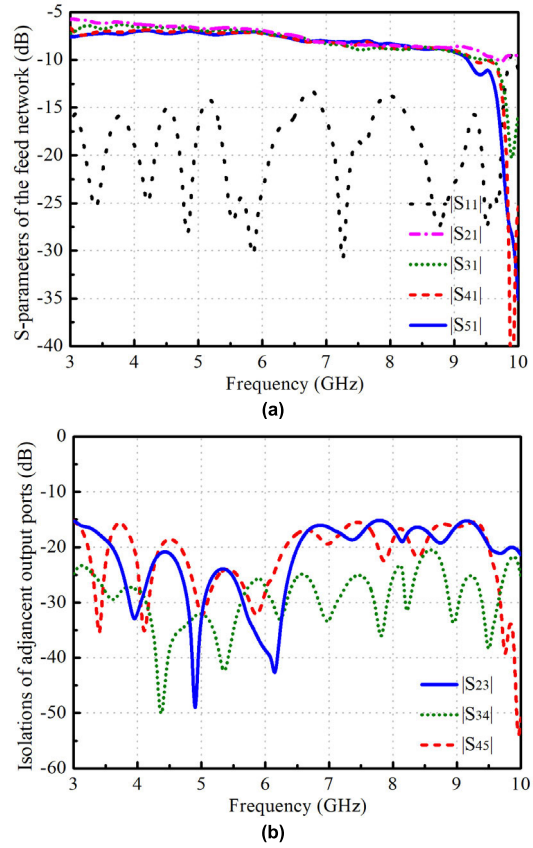

FIGURE 14. Transmission coefficients, reflection coefficients and isolations of the scanning feeding network. (a) transmission coefficients and reflection coefficients. (b) isolations.

($|S_{11}|$) ranging from 2.96 to 10.68GHz and its transmission coefficients ($|S_{21}|$, $|S_{31}|$) present a variation of 0.03dB. Additionally, the isolation between two output ports is larger than 15dB. All results indicate that this divider can be used for wideband system.

According to the sketch map in Fig. 6, a frequency scanning feeding network, which is composed of two conventional TLs, four FCIDC-based CRLH TLs and three wideband Wilkinson power dividers, is synthesized. Among four CRLH TLs, three of them are TL2 and one of them is TL3.

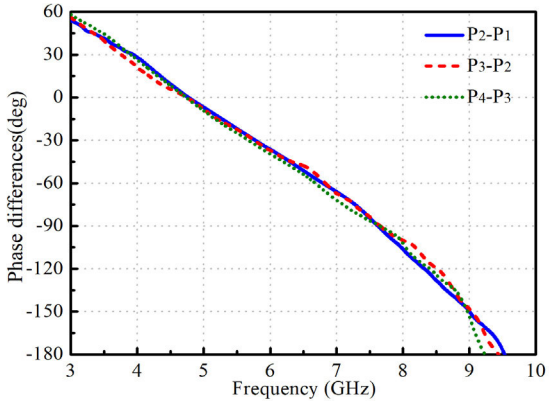

FIGURE 15. Phase differences between the adjacent output ports.

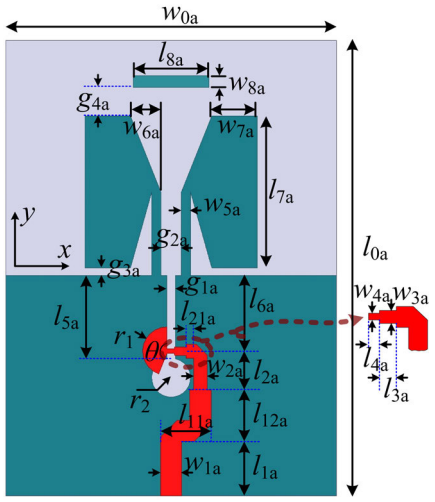

FIGURE 16. Structure of planar quasi-Yagi antenna element.

Fig. 14 depicts the magnitude responses of the designed network. $|S_{21}|$, $|S_{31}|$, $|S_{41}|$ and $|S_{51}|$ are the transmission coefficients for output ports 2, 3, 4 and 5. It can be observed that the transmission coefficients of synthesized network are 7.5±1.5dB and the reflection coefficients are less than −13dB from 3 GHz to 9 GHz. Besides, the isolations of the output ports are less than −15dB in this band.

Fig. 15 shows the phase differences of the adjacent output ports. The phase differences of adjacent output ports ($P_i - P_{i-1}$, $i = 2, 3, 4$) are 0° at 4.7 GHz. At 3 GHz, the phase differences are 48.6°, 50.2°, 52.1° for P_2-P_1, P_3-P_2, P_4-P_3. And at 9 GHz, the phase differences are -149.81°, -147.92°, -152.12° for P_2-P_1, P_3-P_2, P_4-P_3. The magnitude and phase responses are suitable for the index of the target frequency-scanning phased-array feeding network.

IV. TIGHTLY COUPLED PLANAR QUASI-YAGI ANTENNA ARRAY

Quasi-Yagi antenna, which has advantages of excellent linearly polarization, small occupied size and wide band, provides a good choice for the wideband frequency-scanning

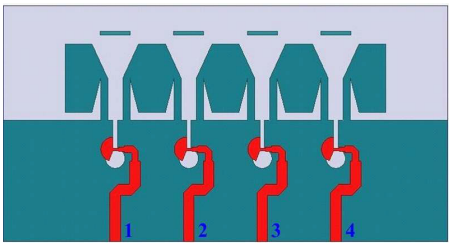

FIGURE 17. Tightly coupled planar quasi-Yagi antenna array.

operation. Recently, tightly coupled planar quasi-Yagi antenna has been extensively studied for phased array, because large scanning angle in wideband can be realized by using this technique.

Fig. 16 presents the topology of the quasi-Yagi antenna element. Due to the intrinsic characteristic of the slot line to microstrip transition, the out-of-phase power division is realized in wideband frequency. The dimensions of the structure are: $w_{0a} = 59.5$mm, $l_{0a} = 61.75$mm, $w_{1a} = 2.8$mm, $l_{1a} = 12.2$mm, $l_{11a} = 8.05$mm, $l_{12a} = 8.8$mm, $w_{2a} = 1.7$mm, $l_{2a} = 3.15$mm, $l_{21a} = 1.7$mm, $w_{3a} = 1.1$mm, $l_{3a} = 1.5$mm, $w_{4a} = 0.6$mm, $l_{4a} = 1.5$mm, $r_1 = 3.2$mm, $r_2 = 2.5$mm, $l_{5a} = 7.5$mm, $l_{6a} = 7.6$mm, $g_{1a} = 1.2$mm, $g_{2a} = 4$mm, $g_{3a} = 2$mm, $w_{5a} = 2$mm, $w_{6a} = 4.2$mm, $w_{7a} = 7.1$mm, $l_{7a} = 18$mm, $w_{8a} = 1$mm, $l_{8a} = 8$mm, $g_{4a} = 2.3$mm and $\theta = 160°$. Fig. 17 presents the planar quasi-Yagi antenna array. This array is composed of four elements and the arms of these elements are connected directly. The distance between the adjacent elements is 19.5 mm for matching the design principle in Section III.

Fig. 18 illustrates the active voltage standing wave ratio (VSWR) of the antenna array. It can be seen that the VSWRs are less than 1.75 from 2.9 GHz to 9 GHz. The results indicate that the designed array has good impedance matching at every port. Fig. 19 depicts the simulated E-plane and H-plane at 3.5 GHz, 5.5GHz and 7.5GHz. The antenna has front-to-back ratio larger than 13 dB for practical applications and has cross-polarization lower than −17.5dB. Besides, the first side lobe becomes large with the increase of frequency. The consistency of these radiation patterns indicates that the designed antenna array can be used for wideband operation.

V. SYNTHESIS OF FREQUENCY-SCANNING PHASED-ARRAY

By feeding the tightly coupled planar quasi-Yagi antenna array using the designed frequency-scanning feeding network, a frequency-scanning phased-array is simulated, fabricated and measured. Fig. 20 illustrates two photographs of the fabricated wideband frequency scanning feeding network. Fig. 20(a) is its front view and Fig. 20(b) is its back view. The frequency-scanning phased-array was tested by an Anritsu ME7808A network analyzer and a far field measurement system in an anechoic chamber.

Fig. 21 presents the simulated and measured S-parameters of the frequency-scanning phased-array. The measured result

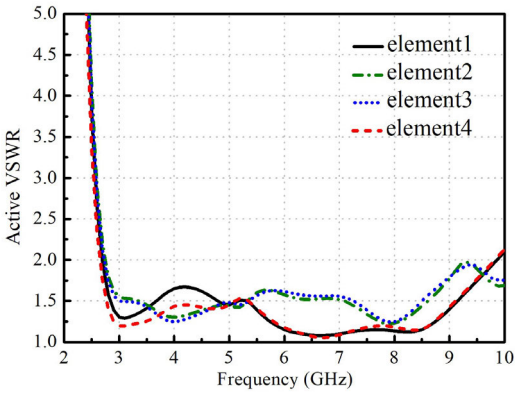

FIGURE 18. Active VSWRs of planar quasi-Yagi antenna array.

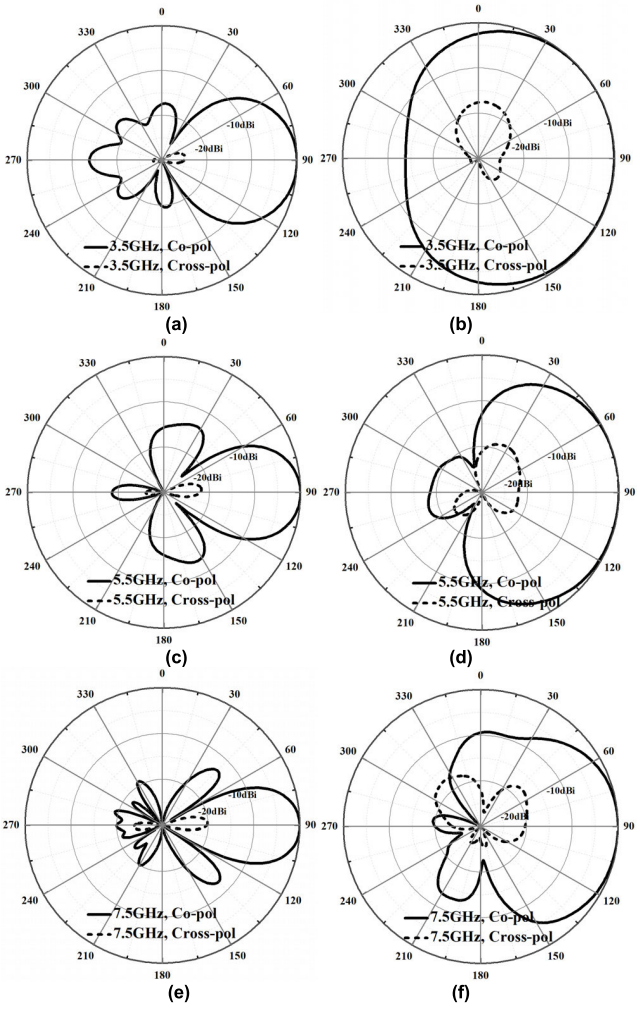

FIGURE 19. Simulated patterns of the tightly coupled quasi-Yagi antenna array. (a) 3.5GHz, E-plane. (b) 3.5GHz, H-plane. (c) 5.5GHz, E-plane. (d) 5.5GHz, H-plane. (e) 7.5GHz, E-plane. (f) 7.5GHz, H-plane.

shows that the reflection coefficient of the antenna array is smaller than −10dB ranging from 2.55GHz to 10GHz, which matches well with the simulated one.

Fig. 22 plots the simulated and measured E-plane scanning radiation patterns. All the results show good performances

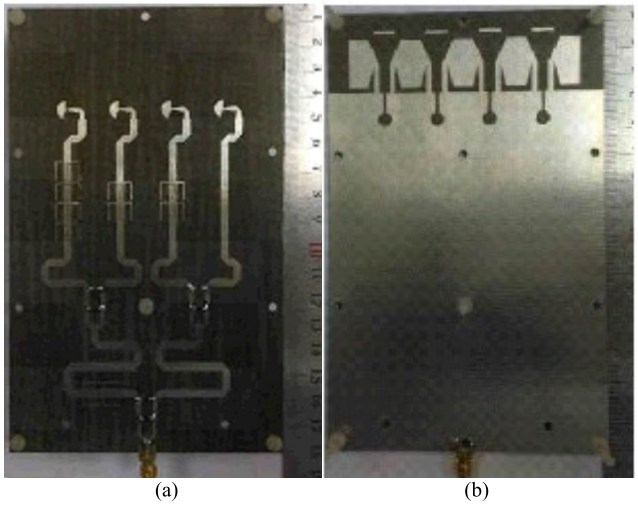

FIGURE 20. Photograph of the fabricated frequency-scanning antenna array. (a) Front view. (b) Back view.

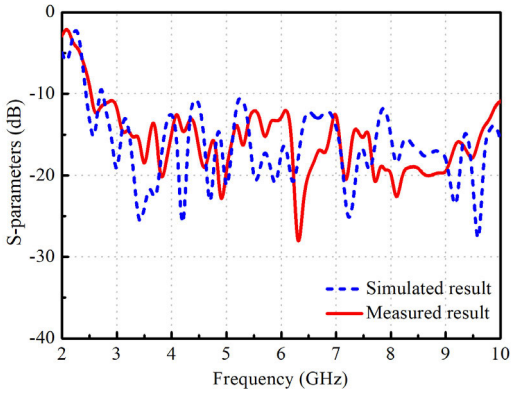

FIGURE 21. Simulated and measured S-parameters of the designed frequency-scanning antenna array.

with the scan angles that agree well with the designed destinations. The measured main beam angles are −47° to 46° between 3GHz and 9GHz, and the corresponding simulated angles are −45° to 45°. In detail, the directions of the main beam angles are −47°, −31°, −14°, 0°, 16°, 29° and 46° for 3GHz, 3.15GHz, 3.7GHz, 4.71GHz, 6.2GHz, 8.1GHz and 9GHz. Although the deviations exist between the simulated results and the measured ones, the fabricated array achieves elevation scanning angles towards both negative and positive.

The far field of an antenna array is equal to the product of the field of a single element, at a selected reference point, and the array factor of this array. In this paper, the antenna array is composed of four uniform quasi-Yagi antenna elements linearly. Generally, the wavelength varies with the frequency. For a single element, the physical sizes are fit and varying quantities of half wavelengths are distributed in different frequencies. If the number of half wavelength is smaller than 1, the currents of the element are in phase. In this case, the efficient currents increase significantly with frequency, which results in the far field stacking in phase. So, the directivity enhances and the half power beam width (HPBW) becomes narrow. If the number of half wavelength is larger than 1,

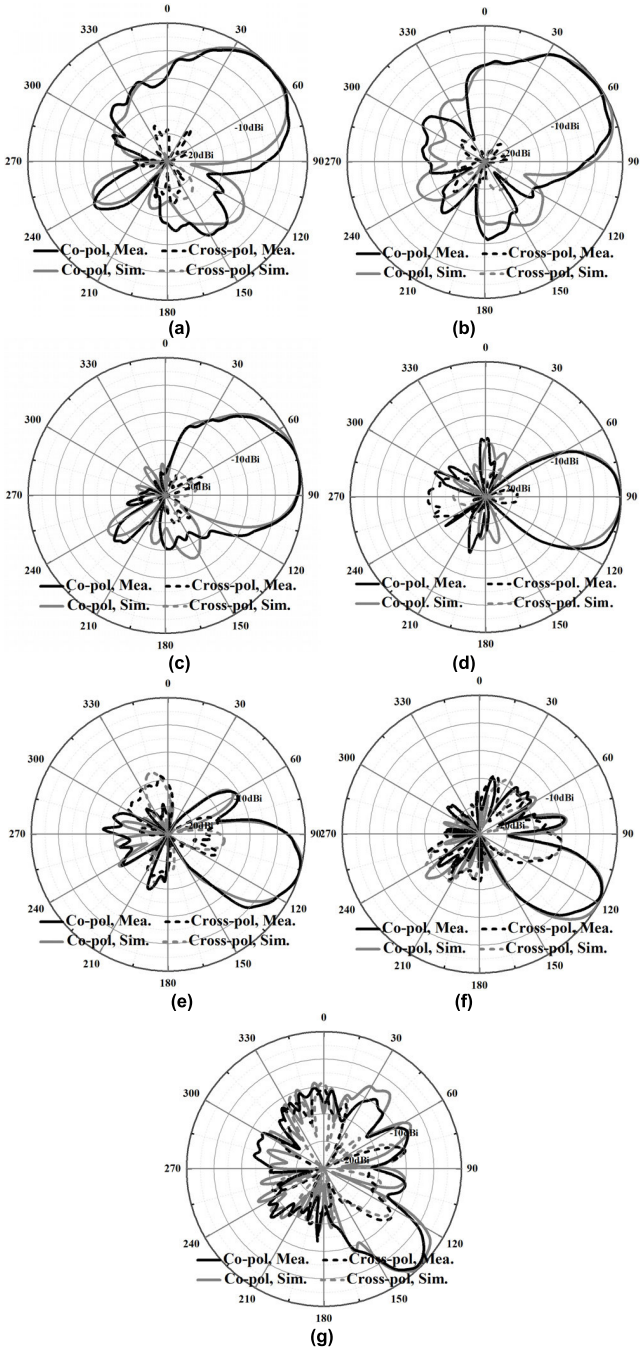

FIGURE 22. Simulated and measured radiation patterns of the designed frequency-scanning antenna array. (a) 3GHz, −45°. (b) 3.15GHz, −30°. (c) 3.7GHz, −15°. (d) 4.7GHz, 0°. (e) 6.2GHz, 15°. (f) 8.1GHz, 30°. (g) 9GHz, 45°.

part of the currents is out of phase, and energy in certain directions is cancelled. As a result, the pattern nulls generate and side lobes appear. The number of half wavelength has an important influence on the number of side lobes. For a linear array with n uniform elements, its array factor $f_a(\theta)$ can be expressed as

$$|f_a(\theta)| = \left| \frac{\sin\left[\frac{n}{2}(kd\cos\theta + \xi)\right]}{\sin\left[\frac{1}{2}(kd\cos\theta + \xi)\right]} \right| \tag{14}$$

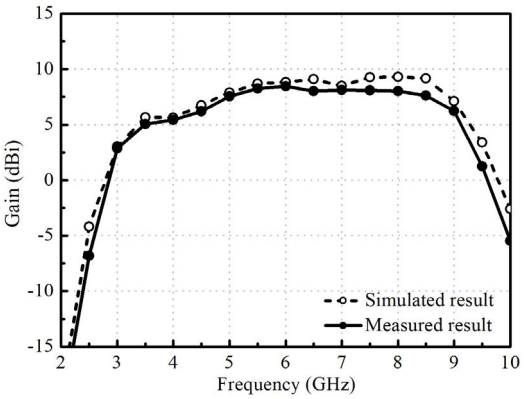

FIGURE 23. Simulated and measured gains of the designed frequency-scanning antenna array.

TABLE 1. Comparison between this work with publications.

	Bandwidth	Beam Angle	Technology
[18]	1.8 to 2.5GHz	about -30° to +30°	Lumped load
[19]	4.76 to 8.26GHz	-50° to +50°	DGS
[20]	1.8GHz/2.5GHz	10°/-9.5°	Lumped load
This work	3 to 9GHz	-47°to +46°	FCIDC

Here, k is the wave number, d is the element spacing and ξ is the phase excitation difference. $kd\cos\theta$ is the wave path difference in the direction of θ. In this design, ξ elevates towards both negative and positive. From the expression, it can be obtained that n-2 side lobes appear and one main beam generates. Based on the above analysis, it can be obtained that the HPBW becomes narrow and more side lobes appear with the increase of frequency.

Fig. 23 presents the simulated and measured gains of the frequency-scanning phased-array. It can be seen that the measured gains are lower than those of simulated ones in the same frequencies, and they are also lower than gains of the tightly coupled antenna array without feeding network.

To validate the advancement of this design, Table 1 presents the comparison between this work and other publications. It can be seen that this design has a wide band and a large scanning angle, which indicates that it can be used in those systems requiring wide scanning angle in wide band. Although the dual-layer technique is used, it can be manufactured by adopting the method of one-time forming technique. So, it can avoid the artificial error introduced by the methods of lumped loaded. Besides, it can avoid the encapsulation difficulty of defected ground structure (DGS).

The reasons of scanning angles deviation and gain decreasing can be concluded as: (1) The insertion loss of the feeding network becomes large with the frequency increasing (as shown in Fig. 14(a)). (2) The phase inconsistency of the feeding network results in the phenomenon that the radiation of the antenna elements can't be realized in-phase stack. (3) The loss of the substrate and the assembly error also can cause the amplitude/phase error.

VI. CONCLUSION

In this paper, a frequency-scanning feeding network is designed, fabricated and measured. Initially, a novel FCIDC, which can realize wide operating band and miniaturization, is proposed. The equivalent circuit model and the dispersion curves are auxiliary instructions to explain the enhanced performances of FCIDC CRLH unit cell. And then, topology of the scanning feeding network is given and its working principle is presented. Based on the topology, a wide band frequency-scanning feeding network is synthesized by CRLH TLs and wideband Wilkinson power dividers. For frequency-scanning phased-array, a tightly coupled antenna array is adopted. Finally, a phased array, which achieves elevation plane scanning towards both negative and positive, is fabricated and measured. The results indicate that the frequency-scanning feeding network has wide scanning angles in wide band. The low profile of microstrip design makes the antenna array have a good potential in conformal requirements.

ACKNOWLEDGMENT

(Bin-Feng Zong and Hui-Yong Zeng contributed equally to this work.)

REFERENCES

[1] D. R. Jackson, P. Baccarelli, P. Burghignoli, A. Galli, and G. Lovat, "Development of leaky-wave antennas," in *Proc. IEEE Int. Symp. Antennas Propag. (APSURSI)*, Fajardo, Puerto Rico, Jun. 2016, pp. 687–688.

[2] R. Shaw and M. K. Mandal, "Backfire microstrip leaky-wave antenna with reduced sidelobe and low cross polarization," *IEEE Antennas Wireless Propag. Lett.*, vol. 18, no. 6, pp. 1218–1222, Jun. 2019.

[3] D.-F. Guan, P. You, Q. Zhang, Z.-H. Lu, S.-W. Yong, and K. Xiao, "A wide-angle and circularly polarized beam-scanning antenna based on microstrip spoof surface plasmon polariton transmission line," *IEEE Antennas Wireless Propag. Lett.*, vol. 16, pp. 2538–2541, 2017.

[4] D. Wei, J. Li, J. Yang, Y. Qi, and G. Yang, "Wide-scanning-angle leaky-wave array antenna based on microstrip SSPPs-TL," *IEEE Antennas Wireless Propag. Lett.*, vol. 17, no. 8, pp. 1566–1570, Aug. 2018.

[5] D. K. Karmokar, Y. J. Guo, P.-Y. Qin, S.-L. Chen, and T. S. Bird, "Substrate integrated waveguide-based periodic backward-to-forward scanning leaky-wave antenna with low cross-polarization," *IEEE Trans. Antennas Propag.*, vol. 66, no. 8, pp. 3846–3856, Aug. 2018.

[6] D.-J. Wei, J. Li, J. Liu, G. Yang, and W. Zhang, "Dual-band substrate-integrated waveguide leaky-wave antenna with a simple feeding way," *IEEE Antennas Wireless Propag. Lett.*, vol. 18, no. 4, pp. 591–595, Apr. 2019.

[7] D. J. Wei, J. Y. Li, J. Liu, G. W. Yang, and W. Zhang, "Dual-band and dual-polarized leaky-wave antenna based on slotted SIW," *IEEE Antennas Wireless Propag. Lett.*, vol. 18, no. 3, pp. 503–511, Mar. 2019.

[8] W. Ma, W. Cao, S. Shi, and X. Yang, "Compact high gain leaky-wave antennas based on substrate integrated waveguide TE220 mode," *IEEE Access*, vol. 7, pp. 145060–145066, 2019.

[9] A. Sarkar, A. Sharma, A. Biswas, and M. J. Akhtar, "EMSIW-based compact high gain wide full space scanning LWA with improved broadside radiation profile," *IEEE Trans. Antennas Propag.*, vol. 67, no. 8, pp. 5652–5657, Aug. 2019.

[10] E. Abdo-Sanchez, M. Chen, A. Epstein, and G. V. Eleftheriades, "A leaky-wave antenna with controlled radiation using a bianisotropic Huygens' metasurface," *IEEE Trans. Antennas Propag.*, vol. 67, no. 1, pp. 108–120, Jan. 2019.

[11] E. Abdo-sanchez, A. Epstein, and G. V. Eleftheriades, "Reconfigurability mechanisms with scanning rate control for omega-bianisotropic Huygens' metasurface leaky-wave antennas," *IEEE Access*, vol. 7, pp. 1–14, 2019.

[12] B. B. Tierney and A. Grbic, "Arbitrary beam shaping using 1-D impedance surfaces supporting leaky waves," *IEEE Trans. Antennas Propag.*, vol. 63, no. 6, pp. 2439–2448, Jun. 2015.

[13] B. B. Tierney and A. Grbic, "Controlling leaky waves with 1-D cascaded metasurfaces," *IEEE Trans. Antennas Propag.*, vol. 66, no. 4, pp. 2143–2146, Apr. 2018.
[14] C. Caloz and T. Itoh, "Array factor approach of leaky-wave antennas and application to 1-D/2-D composite right/left-handed (CRLH) structures," *IEEE Microw. Wireless Compon. Lett.*, vol. 14, no. 6, pp. 274–276, Jun. 2004.
[15] R. Siragusa, E. Perret, P. Lemaitre-Auger, H. Van Nguyen, S. Tedjini, and C. Caloz, "A tapered CRLH Interdigital/Stub leaky-wave antenna with minimized sidelobe levels," *IEEE Antennas Wireless Propag. Lett.*, vol. 11, pp. 1214–1217, 2012.
[16] M. Alibakhshikenari, B. S. Virdee, M. Khalily, P. Shukla, C. H. See, R. Abd-Alhameed, F. Falcone, and E. Limiti, "Beam-scanning leaky-wave antenna based on CRLH-metamaterial for millimetre-wave applications," *IET Microw., Antennas Propag.*, vol. 13, no. 8, pp. 1129–1133, Jul. 2019.
[17] T. Ueda, Y. Kubo, T. Kaneda, M. Hara, Y. Takahashi, and T. Itoh, "Dispersion-free and tunable nonreciprocities in composite right-/left-Handed metamaterials and their applications to beam squint reduction in leaky-wave antennas," *IEEE Trans. Microw. Theory Techn.*, vol. 67, no. 6, pp. 2227–2237, Jun. 2019.
[18] J. H. Choi, J. S. Sun, and T. Itoh, "Frequency-scanning phased-array feed network based on composite right/left-handed transmission lines," *IEEE Trans. Microw. Theory Techn.*, vol. 61, no. 8, pp. 3148–3157, Aug. 2013.
[19] J. H. Choi and T. Itoh, "Dual-band composite Right/Left-handed (CRLH) phased-array antenna," *IEEE Antennas Wireless Propag. Lett.*, vol. 11, pp. 732–735, 2012.
[20] B.-F. Zong, G. Wang, D. Wang, X. Zhang, and J. Liang, "Wideband frequency-scanning phased-array feed network using novel composite right/left-handed unit cell," *Electron. Lett.*, vol. 52, no. 1, pp. 55–57, Jan. 2016.
[21] M. D. Enders, J. H. Choi, and J. K. Lee, "Integrated full-hemisphere space-to-frequency mapping antenna with CRLH stripline feed network," *IEEE Trans. Microw. Theory Techn.*, vol. 66, no. 11, pp. 4765–4772, Nov. 2018.
[22] F. P. Casares-Miranda, E. Márquez-Segura, P. Otero, and C. Camacho-Peñalosa, "Composite right/left-handed transmission line with wire bonded interdigital capacitor," *IEEE Microw. Wireless Compon. Lett.*, vol. 16, no. 11, pp. 624–626, Nov. 2006.
[23] C. Caloz, H. Okabe, T. Iwai, and T. Itoh, "Transmission line approach of left-handed (LH) materials," in *Proc. USNC/URSI Nat. Radio Sci. Meeting*, San Antonio, TX, USA, 2002, p. 39.
[24] R. Mongia, I. J. Bahl, and P. Bhartia, *RF and Microwave Coupled-Line Circuits*. Norwell, MA, USA: Artech-House, 1999.
[25] C. Caloz and T. Itoh, *Electromagnetic Metamaterials: Transmission Line Theory and Microwave Applications*. New York, NY, USA: Wiley, 2005.
[26] D. M. Pozar, *Microwave Engineering*. New York, NY, USA: Wiley, 2005.
[27] X.-J. Zou, G.-M. Wang, Y.-W. Wang, and H.-P. Li, "An efficient decoupling network between feeding points for multielement linear arrays," *IEEE Trans. Antennas Propag.*, vol. 67, no. 5, pp. 3101–3108, May 2019.
[28] D. Parker and D. C. Zimmermann, "Phased arrays—Part 1: Theory and architectures," *IEEE Trans. Microw. Theory Techn.*, vol. 50, no. 3, pp. 678–687, Mar. 2002.